

Dec. 10

- Stress tensor in Granular system
- Theory of Giant Magnetoresistance (Valet and Fert)
- Ferromagnetism in Carbon and Germanium films (Dr. Liou Yung)

Jan. 7

- 0D system: Development of non-carbon based buckyballs and their properties.
- 1D system : Physical properties in stuffed (peapod) carbon nanotube
- 2 D system : The future of graphene electronics and its recent progress

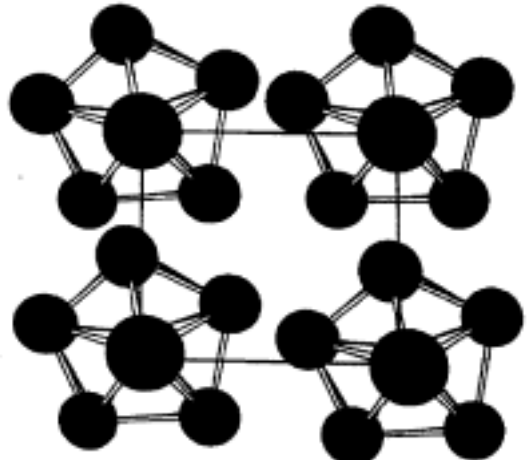
## **6 Bulk Nanostructured Materials**

### **6.1 Solid Disordered Nanostructures 133**

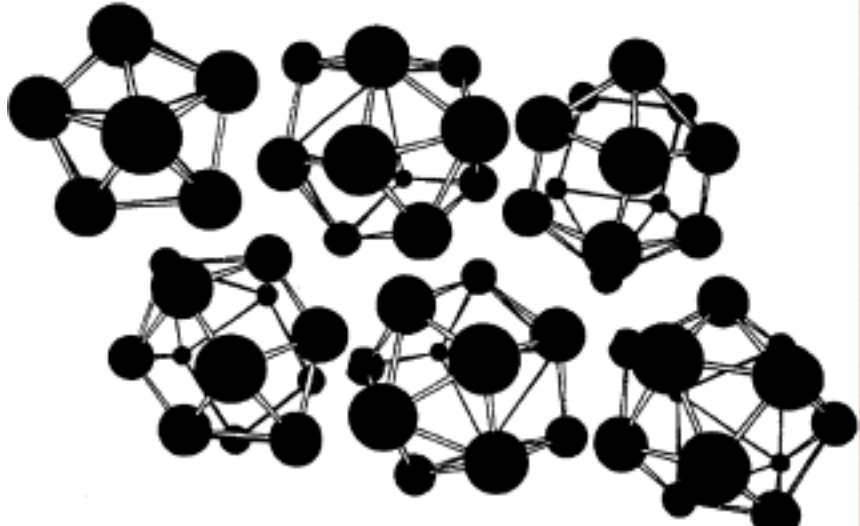
- 6.1.1 Methods of Synthesis 133**
- 6.1.2 Failure Mechanisms of Conventional Grain-Sized Materials 137**
- 6.1.3 Mechanical Properties 139**
- 6.1.4 Nanostructured Multilayers 141**
- 6.1.5 Electrical Properties 142**
- 6.1.6 Other Properties 147**
- 6.1.7 Metal Nanocluster Composite Glasses 148**
- 6.1.8 Porous Silicon 150**

### **6.2 Nanostructured Crystals 153**

- 6.2.1 Natural Nanocrystals 153**
- 6.2.2 Computational Prediction of Cluster Lattices 153**
- 6.2.3 Arrays of Nanoparticles in Zeolites 154**
- 6.2.4 Crystals of Metal Nanoparticles 157**
- 6.2.5 Nanoparticle Lattices in Colloidal Suspensions 158**
- 6.2.6 Photonic Crystals 159**



(a)



(b)

**Figure 6.1.** (a) Illustration of a hypothetical two-dimensional square lattice of  $\text{Al}_{12}$  particles, and (b) illustration of a two-dimensional bulk solid of  $\text{Al}_{12}$  where the nanoparticles have no ordered arrangement with respect to each other.

# Fabrication or synthesis

## For industry, for research

- Compaction and consolidation
- Chill block melt spinning  
    Fig. 6.4
- Gas atomization  
    Fig. 6.5
- MBE
- MOCVD
- Sputter deposition
- Laser ablation
- Self assembly

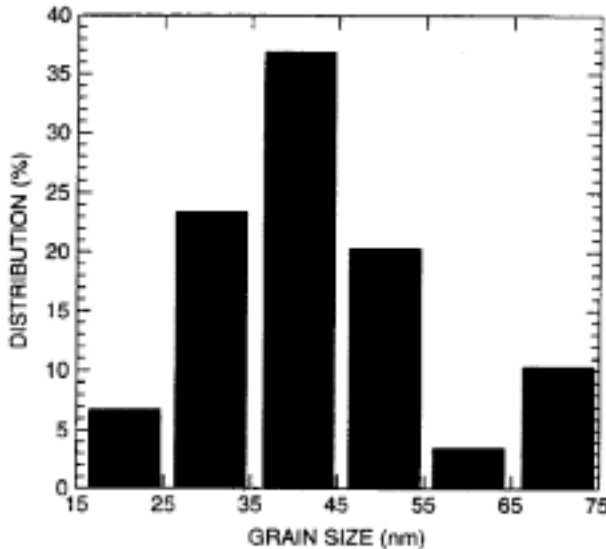


Figure 6.2. Distribution of sizes of Fe-Cu nanoparticles made by hot compaction methods described in the text. [Adapted from L. He and E. Ma, *J. Mater. Res.* 15, 904 (2000).]

## • Mechanical properties

Tension on materials causes elongation and fractures, stress builds up on the cracks and breaks bonds. Edge and screw dislocations cause weak bonds. Grain boundary stops crack propagation.

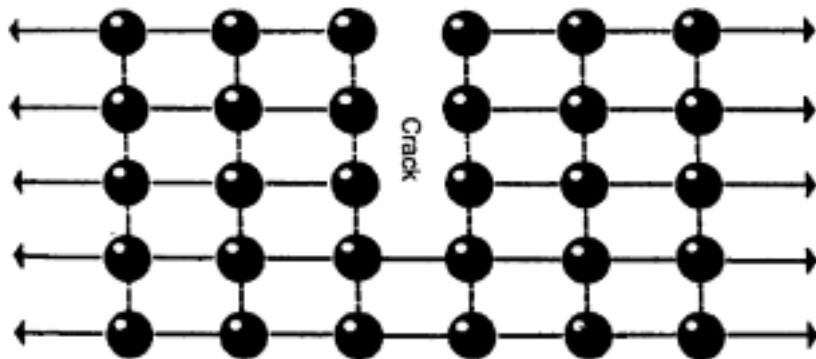


Figure 6.6. A crack in a two-dimensional rectangular lattice.

Brittle-to ductile transition

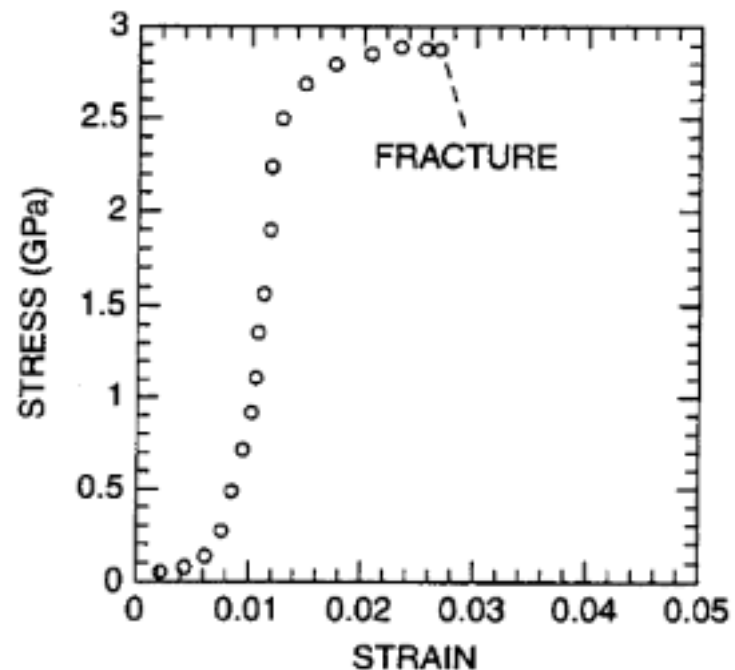
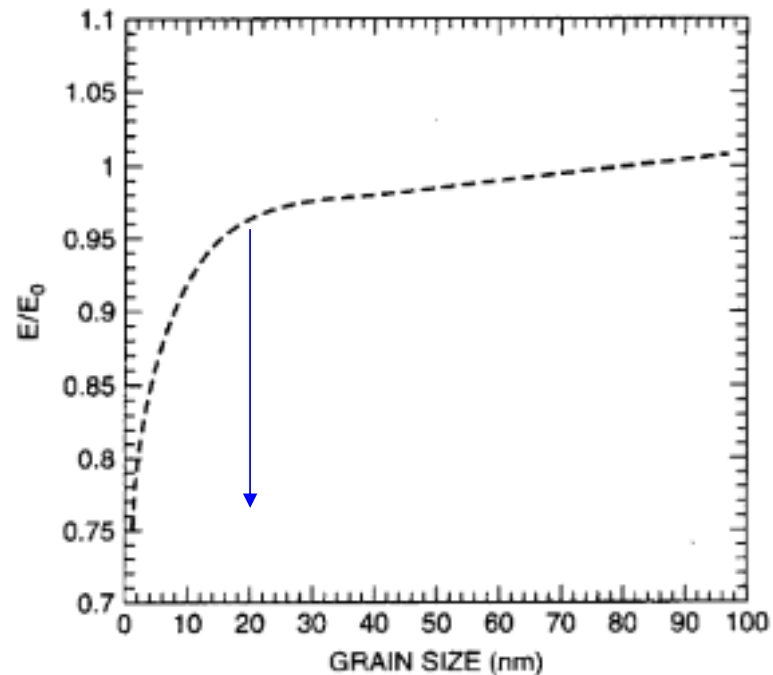


Figure 6.3. Stress-strain curve for bulk compacted nanostructured Fe-Cu material, showing fracture at a stress of 2.8 GPa. [Adapted from L. He and E. Ma, *J. Mater. Res.* 15, 904 (2000).]



**Figure 6.8.** Plot of the ratio of Young's modulus  $E$  in nanograin iron to its value  $E_0$  in conventional granular iron as a function of grain size.

Stress  $S = W / A$  weight per unit cross-section

Strain  $e = \Delta L / L$

$S = E e$  Hook's law

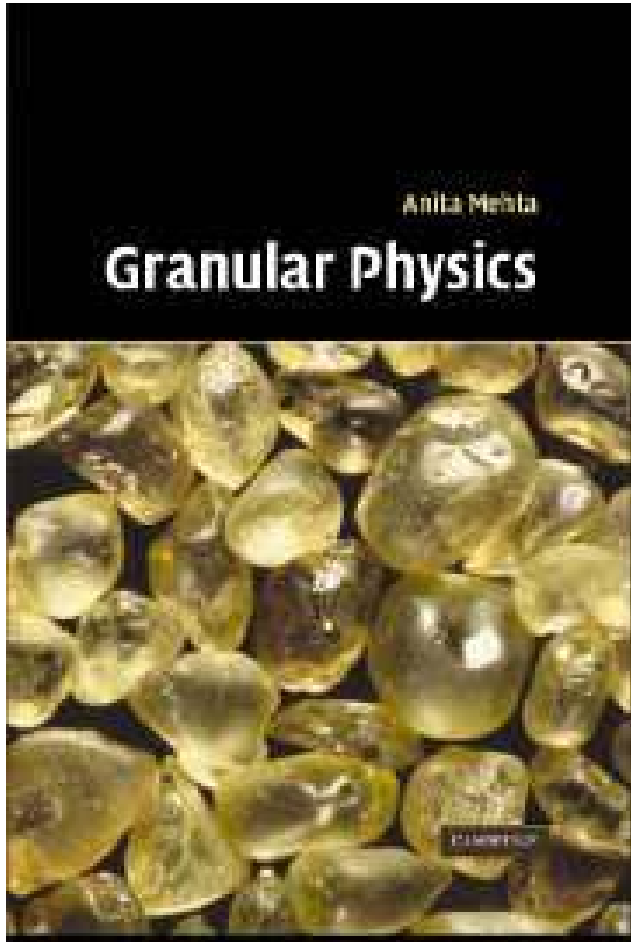
$E = L W / A \Delta L$  Young's modulus  
materials which have smaller  
 $E$  are more elastic

Hall-Petch equation

$$\sigma_y = \sigma_0 + k d^{-1/2}$$

$\sigma_0$  frictional stress opposing dislocation

Fig. 6.9 This works from bulk materials down to  $d \sim 1 \mu\text{m}$



- 13 The thermodynamics of granular materials  
Sir Sam Edwards and Raphael Blumenfeld
- 13.1 Introduction
- 13.2 Statistical mechanics
- 13.3 Volume functions and forces in granular systems
- 13.4 The stress field
- 13.5 Force distribution
- 14 Static properties of granular materials  
Philippe Claudin
- 14.1 Statics at the grain scale
- 14.2 Large-scale properties
- 14.3 Conclusion

## • Multilayers

Mismatch between different layers at the interfaces enhances hardness.

Hardness can be measured by a Nano-indenter.

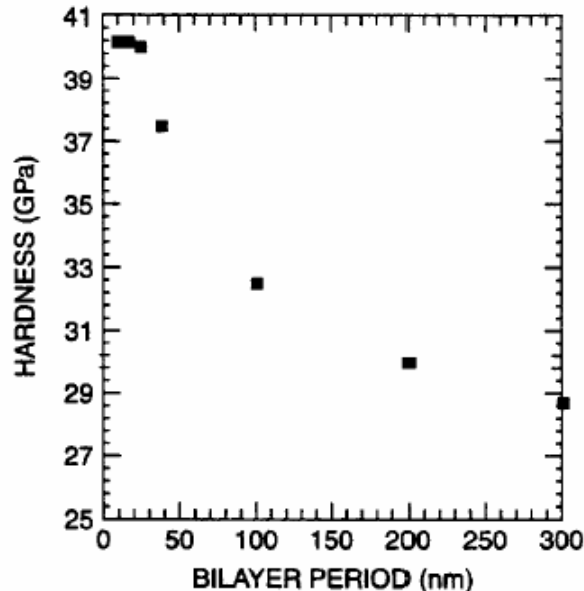


**Figure 6.11.** Plot of the hardness of TiN/NbN multilayer materials as a function of the thickness of the layers. (Adapted from B. M. Clemens, MRS Bulletin, Feb. 1999, p. 20.)

# • Electrical properties

Au nano-particles electrically connected by long thiol molecules.

$$G = G_0 \exp \left( -E / k_B T \right)$$

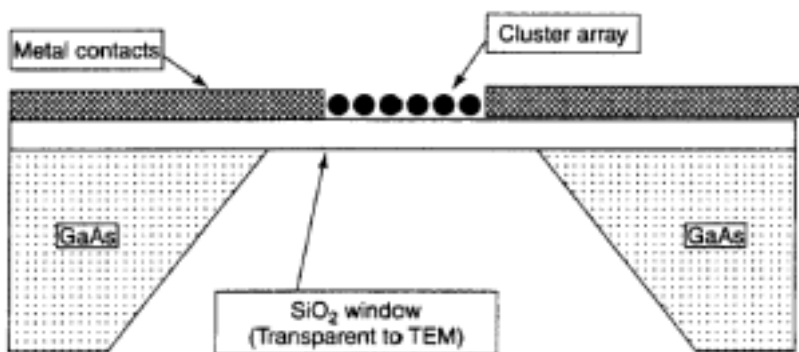


**Figure 6.12.** Cross-sectional view of a lithographically fabricated device to measure the electrical conductivity in a two-dimensional array of gold nanoparticles linked by molecules. (With permission from R. P. Andres et al., in *Handbook of Nanostructured Materials and Nanotechnology*, H. S. Nalwa, ed., Academic Press, San Diego, 2000, Vol. 3, Chapter 4, p. 217.)

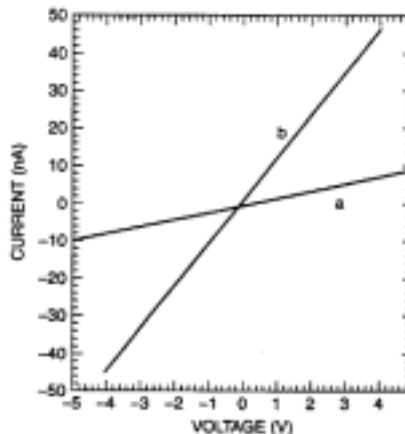


**Figure 6.13.** Room-temperature current-voltage relationship for a two-dimensional cluster without linkage (line a) and with the particles linked by a  $(CN)_2C_6H_4$  molecule (line b). [Adapted from D. James et al., *Superlatt. Microstruct.* 18, 275 (1995).]

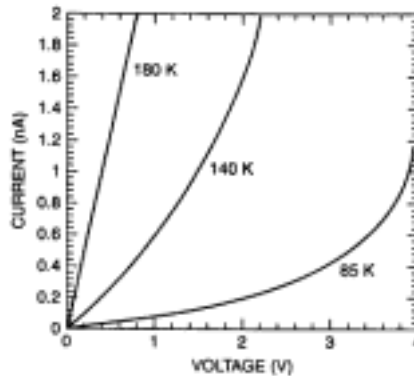


**Figure 6.14.** Measured current-voltage relationship for a two-dimensional linked cluster array at the temperatures of 85, 140, and 180 K. [Adapted from D. James et al., *Superlatt. Microstruct.* 18, 275 (1995).]

Abeles, B., Sheng, Ping, Coutts, M. D. and Arie, Y. (1975)  
'Structural and electrical properties of granular metal films', Advances in  
Physics, 24:3, 407 - 461

## Structural and electrical properties of granular metal films

By B. ABELES, PING SHENG, M. D. COUTTS and Y. ARIE  
RCA Laboratories, Princeton, New Jersey 08540, U.S.A.

[Received 20 January 1975]

### ABSTRACT

Granular metal films (50–200,000 Å thick) were prepared by co-sputtering metals (Ni, Pt, Au) and insulators ( $\text{SiO}_2$ ,  $\text{Al}_2\text{O}_3$ ), where the volume fraction of metal,  $x$ , was varied from  $x=1$  to  $x=0.05$ . The materials were characterized by electron micrography, electron and X-ray diffraction, and measurements of composition, density and electrical resistivity at electric fields  $\mathcal{E}$  up to  $10^6$  V/cm and temperatures  $T$  in the range of 1.3 to 291 K. In the metallic regime (isolated insulator particles in a metal continuum) and in the transition regime (metal and insulator labyrinth structure) the conduction is due to percolation with a percolation threshold at  $x \approx 0.5$ . Tunnelling measurements on superconductor-insulator-granular metal junctions reveals that the transition from the metallic regime to the dielectric regime (10–50 Å size isolated metal particles in an insulator continuum) is associated with the breaking up of a metal continuum into isolated metal particles. In the dielectric regime the temperature dependence of the low-field resistivity is given by  $\rho_L = \rho_0 \exp [2\sqrt{(C/kT)}]$ , and the field dependence of the high-field, low-temperature resistivity is given by  $\rho_H = \rho_\infty \exp (\mathcal{E}_0/\mathcal{E})$ , where  $\rho_0$ ,  $\rho_\infty$ ,  $C$ , and  $\mathcal{E}_0$  are material constants. A simple theory based on the assumption that the ratio  $s/d$  ( $d$ -metal particle size and  $s$ -separation between particles) is a function only of composition yields expressions for  $\rho(\mathcal{E}, T)$  in excellent agreement with experiment. Furthermore, the theory predicts the experimental finding that the resistivity can be expressed in terms of a universal function of the reduced variables  $kT/C$  and  $\mathcal{E}/\mathcal{E}_0$ . The inter-relationship between all the important physical properties of granular metals and their structure is also discussed.

# • Tunneling process

Temp = 0

$$N_1(E - eV)f(E - eV)[N_2(E)(1 - f(E))]$$

left occupied      right empty

$f$  *Fermi-Dirac distribution*

$$I = I(\rightarrow) - I(\leftarrow) =$$

$$K \int N_1(E - eV)N_2(E)[f(E - eV) - f(E)]dE$$

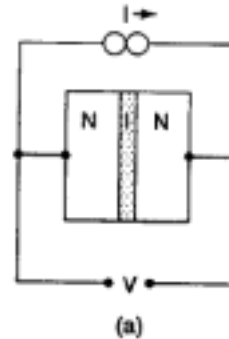
$$= KN_1(E_f)N_2(E_f)eV = G_{nn}V$$

↑

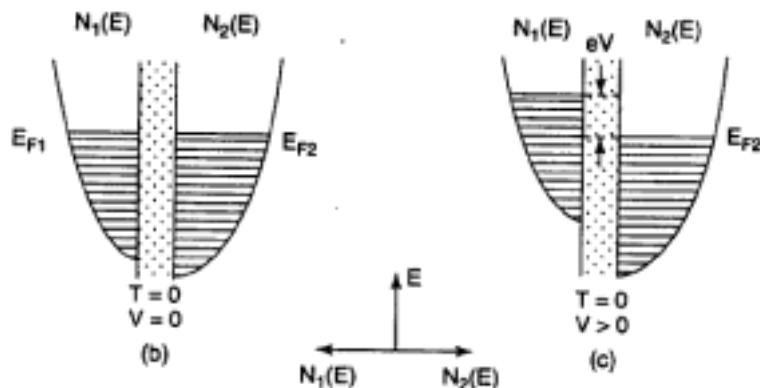
assume constant  $N$ , low  $T$ ,  
small  $V$ , ohmic behavior

$$G_{nn} = KN_1(E_f)N_2(E_f)e$$

conductance



(a)



(b)

(c)

**Figure 6.16.** (a) Metal-insulator-metal junction; (b) density of states of occupied levels and Fermi level before a voltage is applied to the junction; (c) density of states and Fermi level after application of a voltage. Panels (b) and (c) plot the energy vertically and the density of states horizontally, as indicated at the bottom of the figure. Levels above the Fermi level that are not occupied by electrons are not shown.

- Other properties
- Enhanced resistance to oxidation of Fe73B13Si9
  - inherent reactivity depends on numbers of atoms
  - 30 nm Fe(Si) + Fe2B    large interface boundaries
  - FeSi segregates to interface boundaries, diffuses to surface, forms SiO2
- 4 nm In melting T drops to 110 K
- Ic of superconductor increases in Nb3Sn as grain size decreases

## • Optical absorption

- In metallic nanoparticles, the peak wavelength of optical absorption depends on size and material. It is possible to fabricate high-strength transparent metal.

At high frequency, electrons behave like plasma.

For small spherical metal particle embedded in nonabsorbing medium, cluster  $< \lambda$ , well dispersed (non-interacting), absorption coefficient

$$\alpha = \frac{18\pi N_s V n_0 \epsilon_2^3 / \lambda}{[\epsilon_1 + 2n_0^2]^2} + \epsilon_2^2$$

$\epsilon_1, \epsilon_2$  real and imaginary dielectric const of sphere

$N_s$  number of sphere in V

$n_0$  refractive index of insluting glass

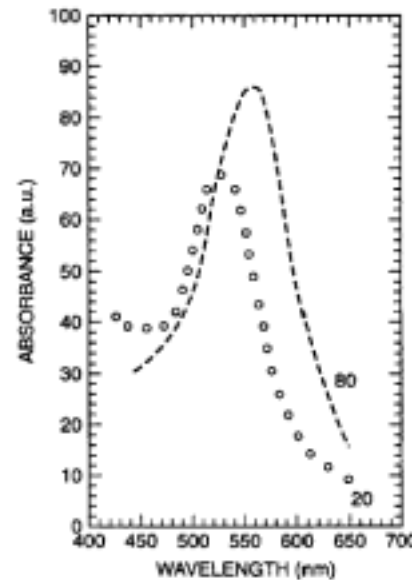


Figure 6.17. Optical absorption spectrum of 20- and 80-nm gold nanoparticles embedded in glass. (Adapted from F. Gonella et al., in *Handbook of Nanostructured Materials and Nanotechnology*, H. S. Nalwa, ed., Academic Press, San Diego, 2000, Vol. 4, Chapter 2, p. 85.)

## Non-linear optical effect

Index of refraction  $n$  depends on intensity --- used as optical switches

For  $n$  having enhanced 3rd order susceptibility,

$$n = n_0 + n_2 I$$

$d < 10$  nm, confinement effect alter absorption properties.

1. Melt
2. Ion implantation  
 $10\text{keV} \sim 10\text{ MeV}$
3. Ion exchange

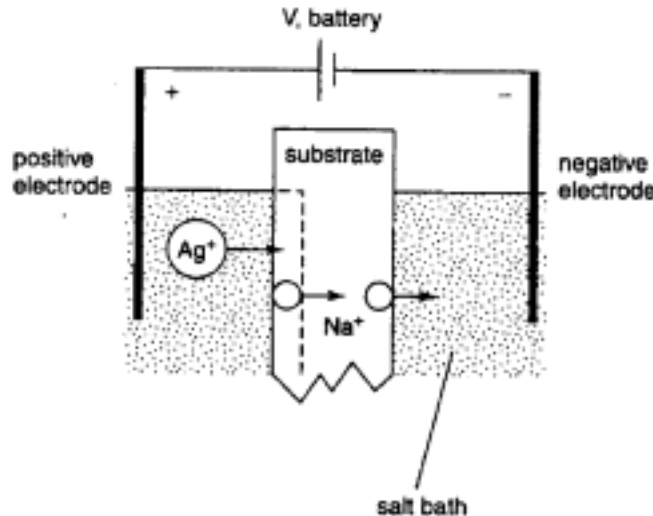


Figure 6.18. Electric field assisted ion exchange apparatus for doping glasses (substrate) with metals such as  $\text{Ag}^+$  ions. [Adapted from G. De Marchi et al., *J. Non-Cryst. Solids* **196**, 79 (1996).]

- Porous Si
- It is interesting because of its fluorescent property at room temp.
  - Luminescence* : matters absorb energy and re-emit energy as visible or near-visible light
  - fluorescent* : absorption and re-emission  $< 10^{-8}$  s
  - phosphorescence* : more delayed emission

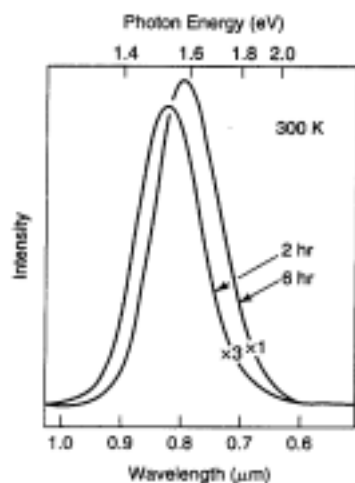


Figure 6.20. Photoluminescence spectra of porous silicon for two different etching times at room temperature. Note the change in scale for the two curves. [Adapted from L. T. Canham, *Appl. Phys. Lett.* 57, 1046 (1990).]

Bandgap  $\sim 1.125$  eV at 300K  
 0.96 – 1.20 eV weak fluorescence

Strong photon-induced luminescence  
 above 1.4 eV

the reason could be  
 oxides on the surface of pores  
 surface defect states  
 quantum wires, dots, and  
 confinement  
 surface state on quantum dots

- Anisotropic etching
  - Porous silicon
  - Fabrication of AFM tips
  - Anodized aluminum oxide (AAO)

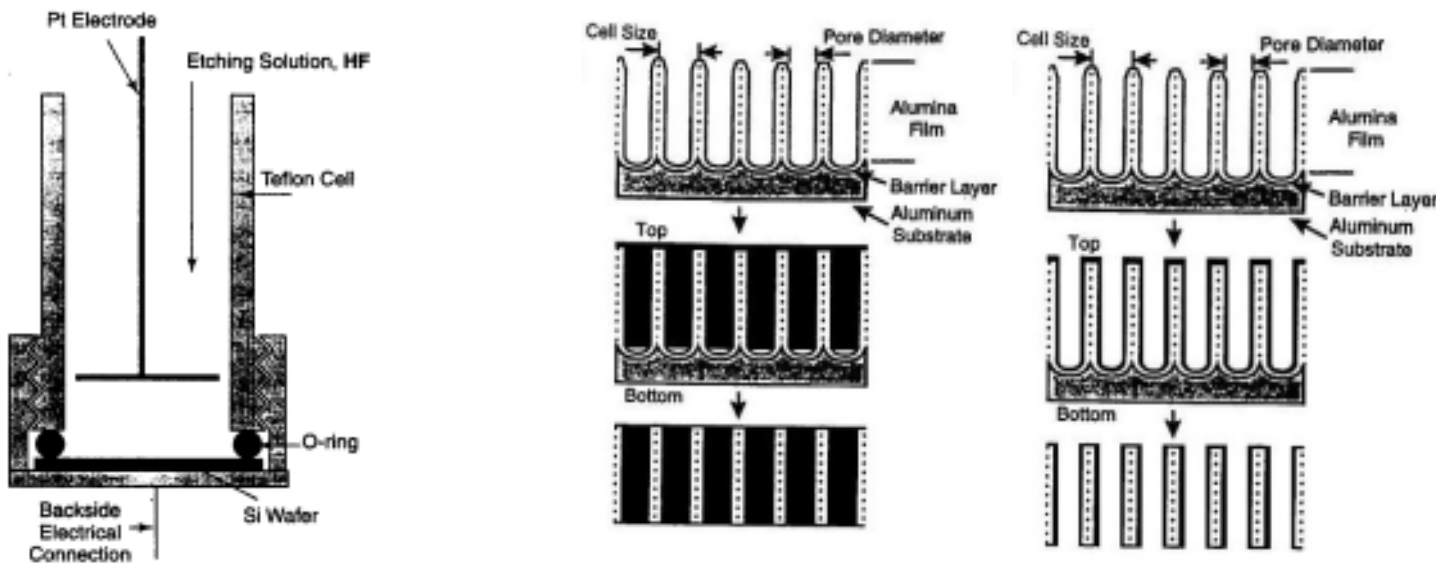
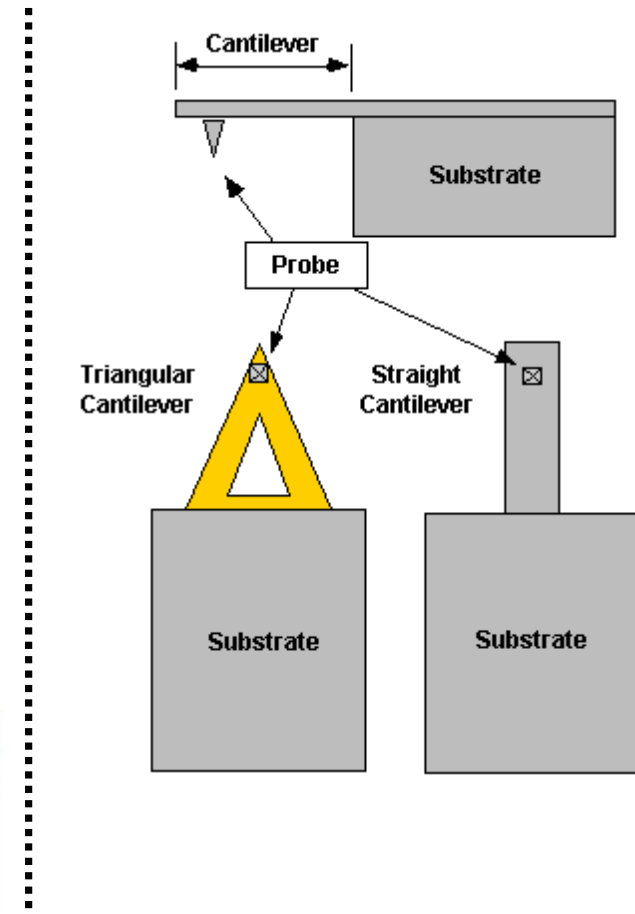
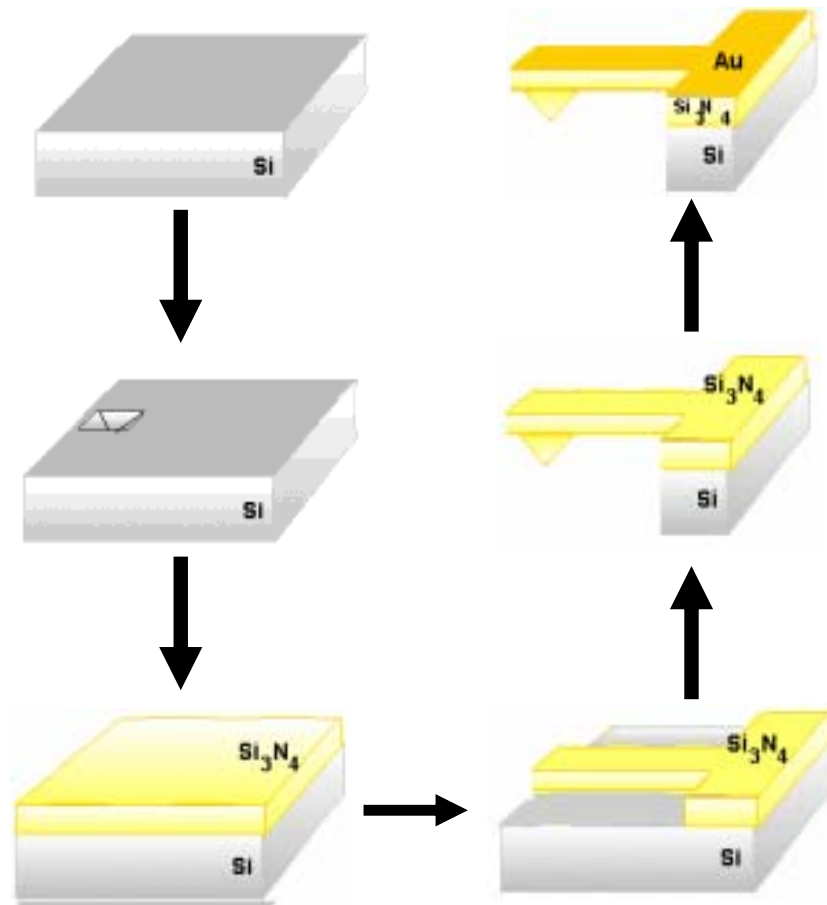
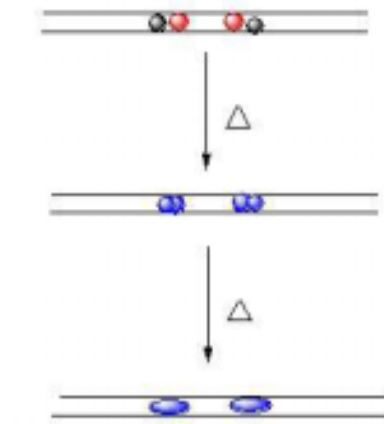
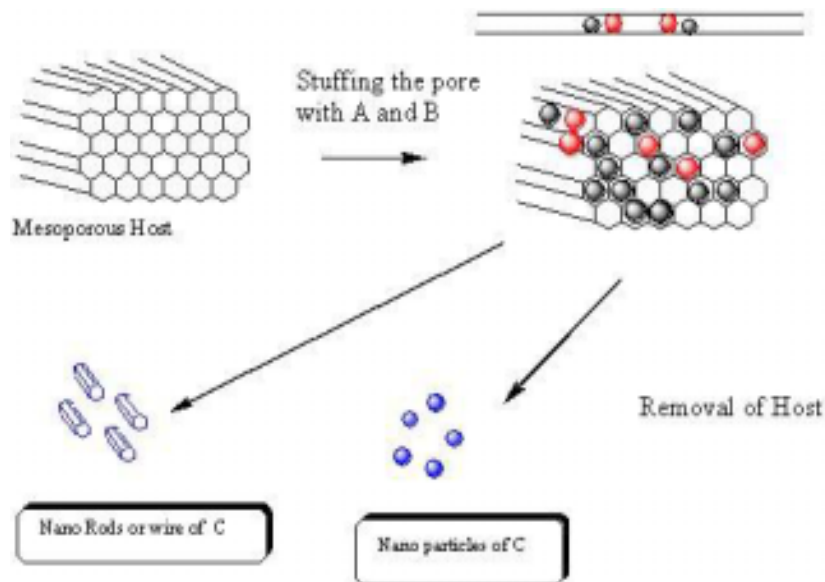


Figure 6.21. A cell for etching a silicon wafer in a hydrogen fluoride (HF) solution in order to introduce pores. (With permission from D. F. Thomas et al., in *Handbook of Nanostructured Materials and Nanotechnology*, H. S. Nalwa, ed., Academic Press, San Diego, 2000, Vol. 4, Chapter 3, p. 173.)

# Fabrication of AFM tips





# Nanostructured crystals

## Natural

$B_{12}$ ,  $C_{60}$

## Artificial

computational predictions

nanoparticles in Zeolites

$Au_m$ ,  $Ag_m$ , Glass, and plastic nanospheres

# Photonic crystal

free electrons in a metal

$$\Psi_{k[r]} = \left[ \frac{1}{V} \right]^{1/3} e^{ik \cdot r}$$

$$p = \hbar k$$

$$k = 2\pi / \lambda$$

$$E = h^2 k^2 / 8\pi^2 m$$

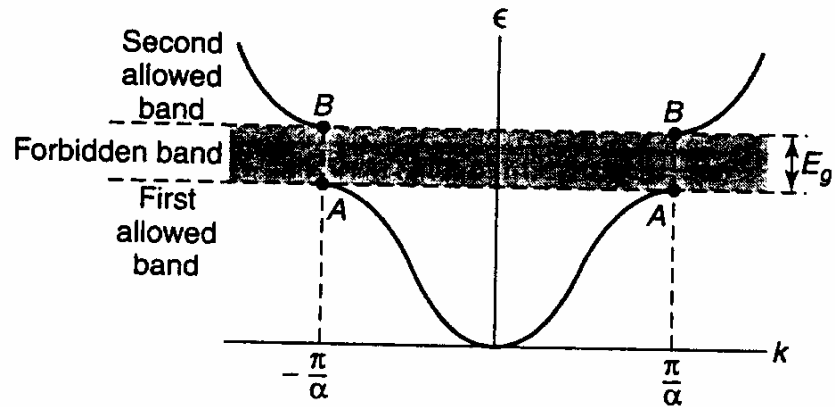


**Figure 6.29.** Curve of energy  $E$  plotted versus wavevector  $k$  for a one-dimensional line of atoms.

$$\nabla^2 H(r) + \epsilon \left[ \frac{\omega^2}{c^2} \right] H(r) = 0$$

$H$  magnetic field of EM radiation  
 $\epsilon$  Dielectric constant (8.9 for  $\text{Al}_2\text{O}_3$ )

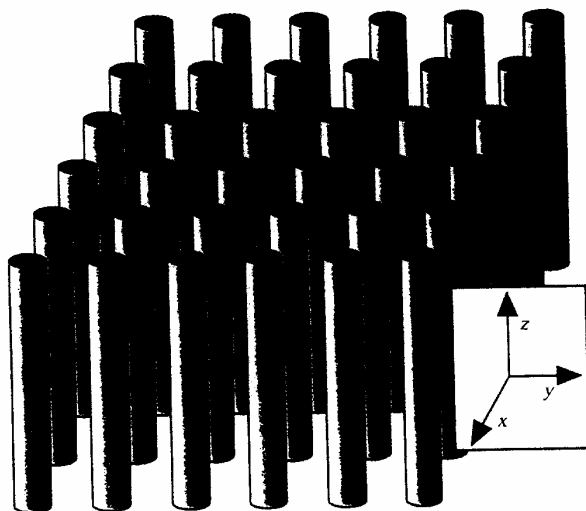


**Figure 6.30.** A two-dimensional photonic crystal made by arranging long cylinders of dielectric materials in a square lattice array.

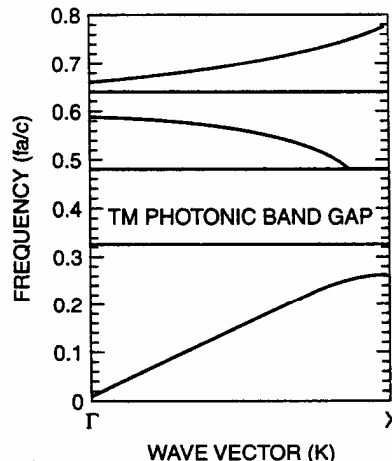


**Figure 6.31.** A part of the dispersion relationship of a photonic crystal mode, TM, of a photonic crystal made of a square lattice of alumina rods. The ordinate scale is the frequency  $f$  multiplied by the lattice parameter  $a$  divided by the speed of light  $c$ . [Adapted from J. D. Joannopoulos, *Nature* **386**, 143 (1997).]

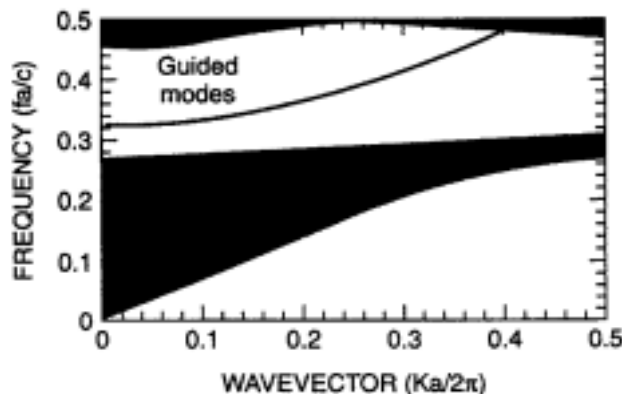


**Figure 6.32.** Effect of removing one row of rods from a square lattice of a photonic crystal, which introduces a level (guided mode) in the forbidden gap. The ordinate scale is the frequency  $f$  multiplied by the lattice parameter  $a$  divided by the speed of light  $c$ . [Adapted from J. D. Joannopoulos, *Nature* **386**, 143 (1997).]

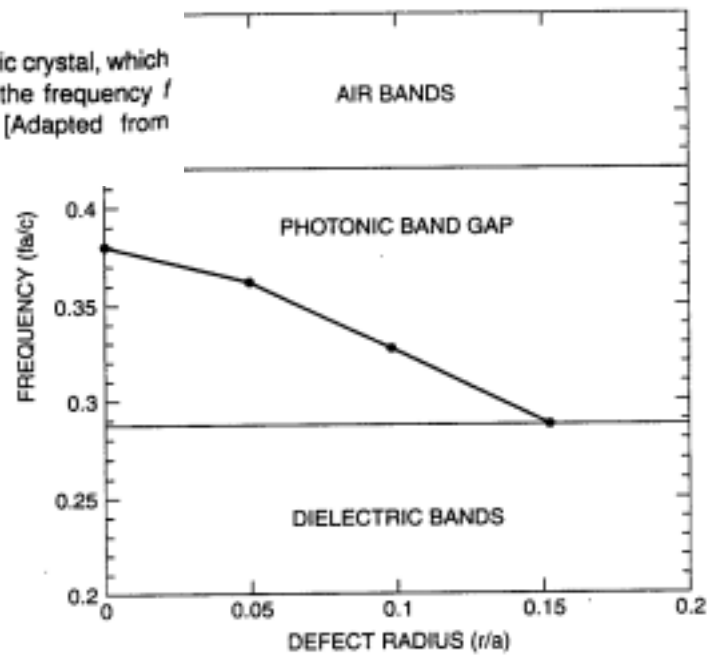


**Figure 6.33.** Dependence of frequency of localized states in the band gap formed on the radius of a single rod in the square lattice. The ordinate scale is the frequency  $f$  multiplied by the lattice parameter  $a$  divided by the speed of light  $c$ . [Adapted from J. D. Joannopoulos, *Nature* **386**, 143 (1997).]

**Fabricating subwavelength array structures using a near-field photolithographic method**

Wei-Lun Chang, Yu-Jen Chang, and Pei-Kuen Weia

*Research Center for Applied Sciences, Academia Sinica, Taipei 11529, Taiwan, Republic of China*

Pei Hsi Tsao

*Department of Physics, National Taiwan University, Taipei 10654, Taiwan, Republic of China*

This work presents a photolithographic approach for producing high aspect ratio arrays in photoresist. The photomask is composed of hexagonal/square rod arrays with a thickness of 0.2 m and a period of 600 nm. Illuminating the photomask with a blue laser generates periodically focused beams up to 1 m long and less than 300 nm wide. A hexagonal rod array provides a better focused beam than a square array due to its higher symmetry. Finite-difference time-domain calculations elucidate the existence of long focused beams above the photomask. Optical near-field measurements verified those subwavelength beams originating from the rod regions. © 2006 American Institute of Physics. DOI:

[10.1063/1.2185249](https://doi.org/10.1063/1.2185249)

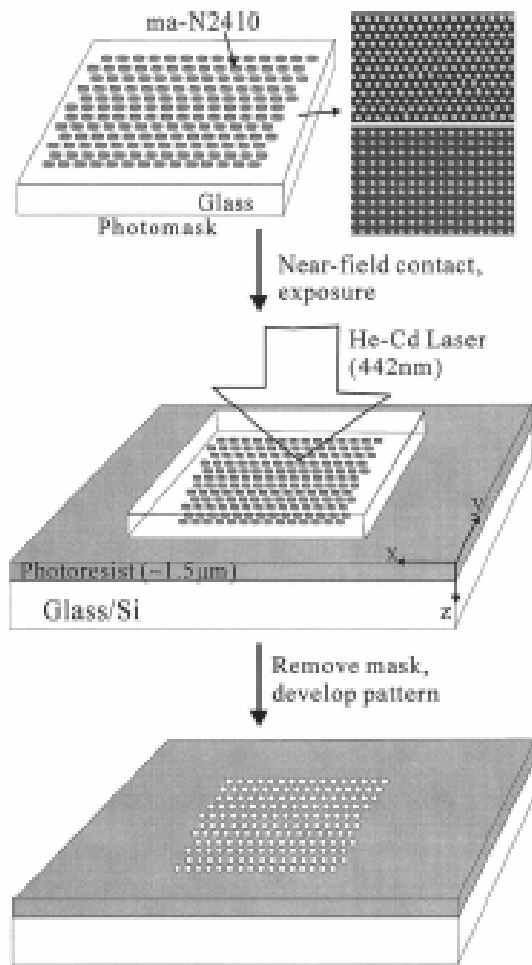


FIG. 1. The experimental setup for the photolithographic process. A transparent photomask comprised of a 2 mm thick glass substrate and a 0.2  $\mu$ m thick air-rod array. Hexagonal and square arrays were made by using electron beam lithography. Both have the same rod diameter (300 nm) and period (60 nm).